This article has been accepted for inclusion in a future issue of this journal. Content is final as presented, with the exception of pagination.

Reinterpreting Low Resistance in Sb–MoS_2 Ohmic Contacts by Means of Ab Initio Transport Simulations

Daniel Lizzit, *Member, IEEE*, Marco Pala, *Senior Member, IEEE*, Francesco Driussi, *Member, IEEE*, and David Esseni, *Fellow, IEEE*

***Abstract*— By using an in-house nonequilibrium Green's function (NEGF)-based ab initio simulator, we investigate the physical mechanisms driving the Sb(01$\bar{1}$2)–MoS_2 system to exhibit the lowest reported contact resistance, $R_C = 42\ \Omega \cdot \mu$m, to the 2-D semiconductor MoS_2. We can find that the transport from the hybridized bands in the Sb–MoS_2 heterojunction is quite ineffective and that the back-gate-induced doping of MoS_2 in the contact region is crucial to explain the experiments. In fact, by accounting in our ab initio simulations for the presence of a back gate according to the experiments, it is possible to match the band structure of the MoS_2 in the Sb–MoS_2 heterojunction with that of the external MoS_2 layer, which drastically increases the electronic transmission throughout the contact, and ultimately pushes R_C close to the quantum limit. Furthermore, we extend the applicability of our previously demonstrated simulation methodology and thus investigate a field-effect transistors (FETs)-like device including an ab initio description of the carrier injection at the Sb–MoS_2 contact.**

***Index Terms*— Antimony, contact resistance, MoS_2, quantum transport, vertical heterojunction (VHJ).**

I. Introduction

IN THE quest for aggressively scaled and highly performing field-effect transistors (FETs), 2-D semiconductors are playing an ever-increasing role [1], [2]. However, their promising intrinsic potentials are often hindered by the high contact resistance (R_C) [3], [4]. This is one of the biggest challenges for 2-D-based FETs, that is unlikely to be solved by resorting to traditional approaches used for 3-D semiconductors. Indeed, the ultrathin nature of monolayer 2-D materials makes them vulnerable to dopant implantation [5], and also techniques for chemical doping based on surface adsorbates are deemed not reliable and effective enough [4], [6].

Among various solutions devised and tested to reduce the R_C to 2-D semiconductors, the use of semimetals with low work function (WF) is arguably the most promising option to reduce R_C in n-type FETs with 2-D semiconductors [7], [8], [9], [10], [11], [12]. This is attributed to a combination of low WF and low density of states (DoS) at the Fermi level (E_F), which leads to a suppression of metal-induced-gap-states (MIGS) close to the MoS_2 conduction band (CB) [12].

The lowest experimentally reported R_C extracted in a 2-D FET device using semimetallic Bi to contact MoS_2 is 123 $\Omega \cdot \mu$m [7]. However, despite the encouraging progress, the low Bi melting point of 271 °C jeopardizes its CMOS process integration. Further steps toward CMOS compatible devices have been achieved using Sb with (0001) surface to contact MoS_2, demonstrating FETs operational after 400 °C thermal treatment, and reporting an R_C of 660 $\Omega \cdot \mu$m [9]. Density functional theory (DFT) simulations extracted the barrier height between Sb and MoS_2; however, no transport simulations were conducted to calculate R_C [9]. An even lower R_C to MoS_2 has been very recently obtained by using Sb contacts with (01$\bar{1}$2) surface orientation, reaching a minimum $R_C = 42\ \Omega \cdot \mu$m at a channel carrier density $n_{2\text{-D}} \approx 3 \times 10^{13}$ cm^{-2} [13], thus approaching the quantum limit resistance of the 2-D semiconductor, namely, 29.6 $\Omega \cdot \mu$m at the above carrier density. Such a low R_C was attributed to the strong overlap between Sb and MoS_2 orbitals in the vertical heterojunction (VHJ), resulting in spatially delocalized hybrid bands with a significant projection onto the MoS_2 orbitals [13]. Upon inspection of DFT calculations for the band structure in the VHJ, Li et al. [13] identified such hybridized states as the crucial aspect enabling a high electronic transmission toward the MoS_2 layer external to the VHJ, ultimately leading to the low R_C. No attempts to calculate R_C in Sb–MoS_2 systems have been reported to date. In this work, for the first time, we present an ab initio transport study of the Sb(01$\bar{1}$2)–MoS_2 system as shown in Fig. 1(a), based on an in-house developed simulator [10], [12], [14], [15].

This article is organized as follows. In Section II, we present the simulation methodology that allows us to perform nonequilibrium Green's function (NEGF) based, quantum transport simulations over large structures and still retain the accurate description of the band structure enabled by ab initio DFT calculations discussed in Section III. In Section IV, we reinterpret the origin of the experimentally obtained low R_C value by inspecting not only the DoSs in the VHJ but also the vertical

Manuscript received 6 November 2023; revised 25 February 2024; accepted 19 March 2024. This work was supported in part by Italian Ministero dell'Università e della Ricerca (MUR) through the Progetti di Rilevante Interesse Nazionale (PRIN) Project under Grant 2017SRYEJH and in part by French Agence Nationale de la Recherche (ANR) through the Tunne2D Project under Grant ANR-21-CE24-0030. The review of this article was arranged by Editor Y. Xu. *(Corresponding author: Daniel Lizzit.)*

The authors are with DPIA, University of Udine, 33100 Udine, Italy (e-mail: daniel.lizzit@uniud.it).

Color versions of one or more figures in this article are available at https://doi.org/10.1109/TED.2024.3381572.

Digital Object Identifier 10.1109/TED.2024.3381572

© 2024 The Authors. This work is licensed under a Creative Commons Attribution 4.0 License.
For more information, see https://creativecommons.org/licenses/by/4.0/

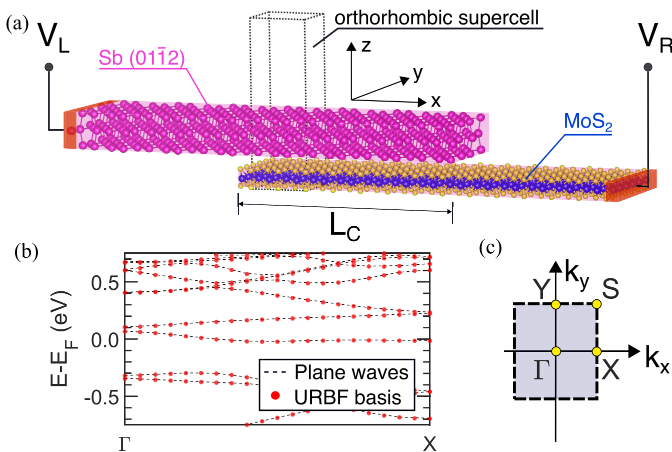

Fig. 1. (a) Overall structure used for DFT and NEGF transport simulations consisting of three regions: the central Sb–MoS_2 VHJ region (having a length L_C), the leftmost Sb region (extending the Sb region of the VHJ), and the rightmost MoS_2 region (extending the MoS_2 region of the VHJ). (b) Band structure of the VHJ along the high-symmetry points shown in (c), and obtained with the reduced URBF basis (symbols) [15], and, compared with the results by QE for a plane waves basis set (dashed lines).

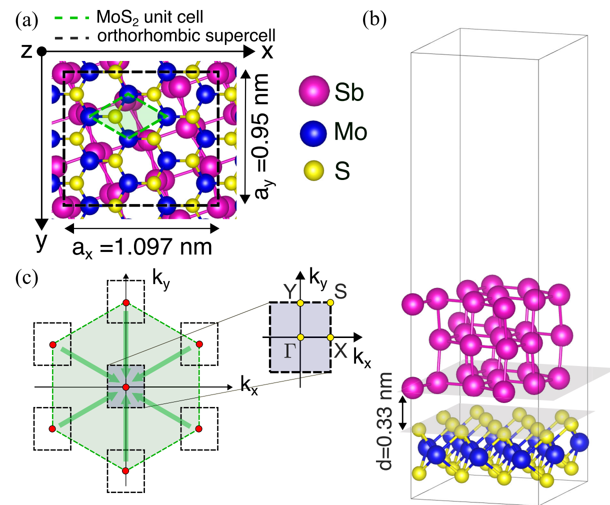

Fig. 2. (a) Top view of the primitive unit cell for MoS_2 (green dashed lines) and the orthorhombic super cell for the VHJ (black dashed lines). (b) Side view of the simulated VHJ, where d is the distance between MoS_2 and Sb with (01$\bar{1}$2) surface orientation. Vacuum is added along the z-direction to reduce the interaction between the periodic replicas of the VHJ in QE calculations. (c) Corresponding first BZs, where the arrows indicate the back folding of the K-points of MoS_2 (for the primitive unit cell) at the Γ point of the first BZ of the supercell.

transmission inside the VHJ (from the Sb to MoS_2), and the lateral transmission from the VHJ to the external MoS_2 layer.

Our results reveal that R_C observed in experiments can only be explained by having MoS_2-type states in the VHJ that match the CB minimum of the external MoS_2 layer, with both minima being close to the Fermi level. We also show that the back-gate biasing (BGB) of the contact region is paramount to attain these conditions. Finally, in Section IV, we use self-consistent simulations, coupling the NEGF equations with the 3-D Poisson's equation, to analyze a FET structure resembling those reported in [13], and comprising an ab initio description of the Sb–MoS_2 contact. The conclusion is drawn in Section V.

II. Simulation Methodology

The Sb(01$\bar{1}$2)–MoS_2 VHJ is simulated with Quantum ESPRESSO (QE) [16], [17] and with an orthorhombic topological symmetry of the VHJ, which is a natural choice for transport calculations [15]. Given the noncommensurate Sb and MoS_2 lattices, we defined a commensurate cell for the VHJ resorting to a procedure well established in the literature [12], [18]. Namely, we matched a strained Sb 2 × 2 unit cell onto an unstrained MoS_2 [Fig. 2(a)] layer, that leads to a mean absolute strain of 4.56% in Sb. To suppress the effects of the spurious replica of the VHJ along z, we introduced a ∼2-nm-thick vacuum region [see Fig. 2(b)], together with the appropriate dipole corrections [17]. The relaxation of atomic positions was reached when the forces acting on each atom were less than 2.5 meV/Å and by setting an energy convergence criteria of 10^{-7} eV. The kinetic energy cutoff was set to 612 eV (45 Ry) and a 12 × 12 × 1 Monkhorst-Pack **k**-point grid was used to sample the Brillouin zone (BZ). We used scalar, relativistic norm-conserving pseudopotentials with generalized gradient approximation (GGA) exchange-correlation approximation. Grimme's DFT-D3 scheme was employed to include the van der waals (vdW) interactions. After the relaxation procedure, the extracted distance between MoS_2 and Sb is 0.33 nm [Fig. 2(b)], which matches with the value obtained on a supercell larger than ours (see Fig. 1 in the extended data of [13]), and it is slightly larger than the ∼0.29-nm value experimentally obtained for the same VHJ by using high-angle annular dark-field scanning transmission electron microscopy (HAADF-STEM) [13].

Quantum transport simulations are performed by means of the NEGF method. Starting from the plane-wave Hamiltonian matrices computed by QE, we extracted Hamiltonian matrices with a reduced order by using a basis set consisting of unit-cell restricted Bloch functions (URBF) [15]. The effectiveness of the URBF basis set in reproducing the band structure of the VHJ obtained with the QE plane-wave Hamiltonians is verified in Fig. 1(b), where it is shown the band structure of the Sb–MoS_2 VHJ close to E_F and along the Γ to X path of Fig. 1(c). For the VHJ used in this work, moving from a plane wave to a URBF basis set allowed us to reduce the Hamiltonian rank by a factor larger than 10^2.

The overall transport simulations used to determine R_C involve three regions [i.e., Sb, VHJ, and MoS_2, as shown in Fig. 1(a)], whose Hamiltonian matrices were first individually extracted. Then, in order to enable transport through the transport direction x, the overall Hamiltonian matrix in the URBF basis was built by using the Hamiltonian matrices coupling the three regions [10], [12].

III. DFT Simulations of the Sb(01$\bar{1}$2)–MoS_2 System

Fig. 3(a) shows the band structure along the high-symmetry points of the orthorhombic VHJ as shown in Fig. 1. The CB minima (CBM) of MoS_2, that in the primitive unit cell are located in the K-points of the first BZ, are back folded at the Γ point of the first BZ of the supercell, as it is indicated by the green arrows in Fig. 2(c). Fig. 3(a) shows that such a minimum (E^{VHJ}_{CBM,MoS_2}) is ≈400 meV above E_F,

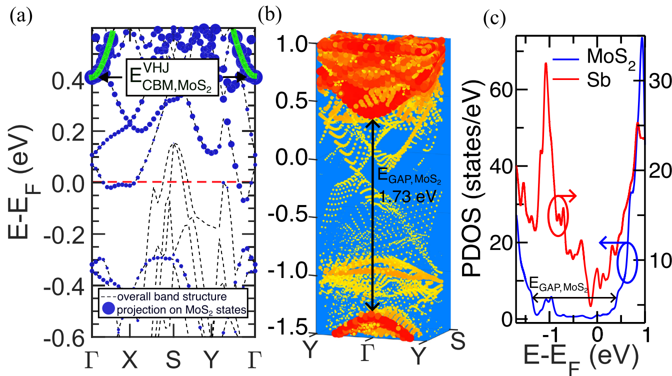

Fig. 3. (a) Band structure of the VHJ along the high-symmetry points shown in Fig. 1(c). Circles indicate the projection on MoS_2 orbitals, and the size of circles is proportional to the weight of the projection. The green line identifies the states in the VHJ corresponding to the CBM of MoS_2 alone, which is back folded at the Γ point in the super cell, as it is shown in Fig. 2(c). (b) Electronic structure of the VHJ projected on MoS_2 orbitals and plotted throughout the first BZ of the supercell. (c) PDOS for MoS_2 (blue line) and Sb (red line). The hybridization between MoS_2 and Sb results in gap states for MoS_2. The semimetallic nature of Sb is identified by the V-shaped DOS near E_F.

so that its contribution to the conductance across the overall heterostructure is negligible in close-to-the-equilibrium bias conditions. The interaction between Sb and MoS_2 also results in the formation of hybridized bands with a significant projection on MoS_2 orbitals that touch or cross E_F. This is in qualitative agreement with the findings in [13], also obtained by means of DFT simulations. However, the band plots cannot be directly compared because of different super cells employed in this work and in [13], leading to different bands folding. Fig. 3(b) reports a 3-D plot throughout the first BZ of the projection onto MoS_2 orbitals of the electronic states in the VHJ that reveals the presence of hybridized states within the MoS_2 energy bandgap. Hybridized states are clearly observed even in the projected DoS (PDOS) in Fig. 3(c) (blue line), where, moreover, the Sb PDOS (red line) confirms the semimetallic nature of Sb that is identified by the typical V-shaped DOS close to E_F [19].

IV. Simulations and Comparison With Experiments

We used ab initio simulations to investigate R_C for the Sb–MoS_2 system in Fig. 1(a), by employing the in-house developed Green-Tea tool [14], [15]. Experimental results for a single layer MoS_2 FET with Sb contacts show an average R_C of about 209 $\Omega \cdot \mu$m at an MoS_2 channel electron density $n_{2\text{-D}} \approx 3 \times 10^{13}$ cm^{-2}, with the lowest reported value being $R_C = 42\ \Omega \cdot \mu$m [13]. By considering the MoS_2 external to the Sb–MoS_2 heterojunction, we analytically converted $n_{2\text{-D}} \approx 3 \times 10^{13}$ cm^{-2} into a band alignment ($E_F - E_{\mathrm{CBM,MoS_2}}$) ≈70 meV, where $E_{\mathrm{CBM,MoS_2}}$ denotes the corresponding MoS_2 CBM. To this purpose, we used an effective mass approximation model with an MoS_2 effective mass, m = 0.44 m_0, and a nonparabolicity coefficient, $\alpha = 0.94$ eV^{-1}, extracted by fitting DFT calculations in a range of ∼200 meV above the CBM.

In Sections IV-A and IV-B, we calculate the close-to-equilibrium R_C in the best case scenario, where, if not otherwise stated, we neglect the band-bending outside the VHJ region and we use the band alignment $(E_F - E_{\mathrm{CBM,MoS_2}}) \approx$ 70 meV for the MoS_2 external to the VHJ.

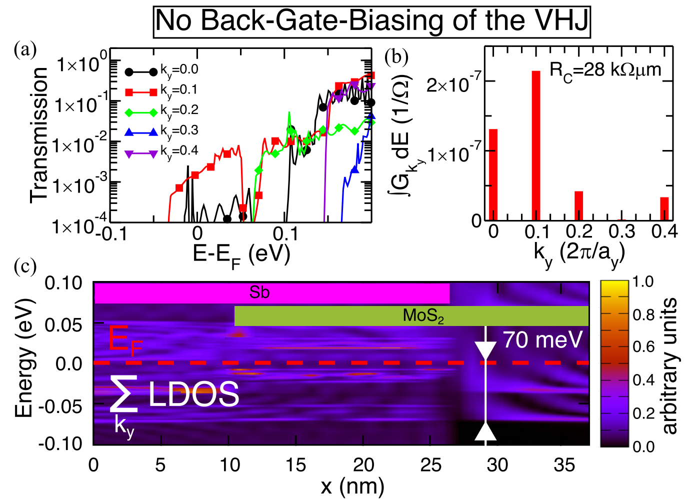

Fig. 4. (a) Electron transmission $T_{k_y}(E)$ versus energy for different transverse wave-vectors k_y that cover almost the entire first BZ. k_y values are in units of $2\pi/a_y$. (b) Calculated values of the integral over the energy defined in (1) for the conductance spectrum. The R_C value resulting from (3) is also shown. (c) LDOS for the system shown in Fig. 1 for a contact length L_C = 15 nm. The alignment with E_F of the CBM for the external MoS_2 layer corresponds to an electron density $n_{2\text{-D}} = 3 \times 10^{13}$ cm^{-2}, which is consistent with the $n_{2\text{-D}}$ value reported in [13].

A. R_C Simulations Neglecting Back-Gate Biasing (BGB)

Fig. 4(a) shows the calculated electronic transmission spectrum at equilibrium for energies close to E_F and for different transverse k_y values. Then, we used the Landauer formula to calculate the linear conductance spectrum $G_{k_y}(E)$ as follows:

$$G_{k_y}(E) = \frac{2q^2}{h} T_{k_y}(E)\left(-\frac{df_0(E - E_F)}{dE}\right) \tag{1}$$

where q is the electron charge, h is Planck's constant, and $f_0(E)$ is the Fermi–Dirac distribution function.

The ballistic equilibrium transmission spectrum $T_{k_y}(E)$, for a given k_y, is computed by using the retarded Green's functions and the contacts self-energies as follows [15]:

$$T(E) = \mathrm{Tr}\big\{[\boldsymbol{\Gamma}_L][\mathbf{G}][\boldsymbol{\Gamma}_R]\big[\mathbf{G}^{\dagger}\big]\big\} \tag{2}$$

where k_y subscript is omitted to lighten the notation. Here, the broadening functions are defined as $[\boldsymbol{\Gamma}_{L(R)}] = i([\boldsymbol{\Sigma}_{L(R)}] - [\boldsymbol{\Sigma}_{L(R)}]^{\dagger})$, where $[\boldsymbol{\Sigma}_{L(R)}]$ is the self-energy of the left (L) or right (R) contact, $[\mathbf{G}]$ is the retarded Green's function of the system, and $\mathrm{Tr}\{\cdots\}$ denotes the trace of a matrix.

Finally, by accounting for the contributions from different transverse k_y values, we obtain R_C as follows:

$$\frac{1}{R_C} = \int_{k_y}\left[\int_{-\infty}^{+\infty} G_{k_y}(E)\, dE\ \right]\frac{dk_y}{2\pi}. \tag{3}$$

As it can be seen, the transmissions in Fig. 4(a) are much smaller than 1.0 close to E_F, and Fig. 4(b) reports k_y resolved contributions to R_C. The overall calculated R_C is about 28 $k\Omega \cdot \mu$m, namely, much larger than the average 209 $\Omega \cdot \mu$m

This article has been accepted for inclusion in a future issue of this journal. Content is final as presented, with the exception of pagination.

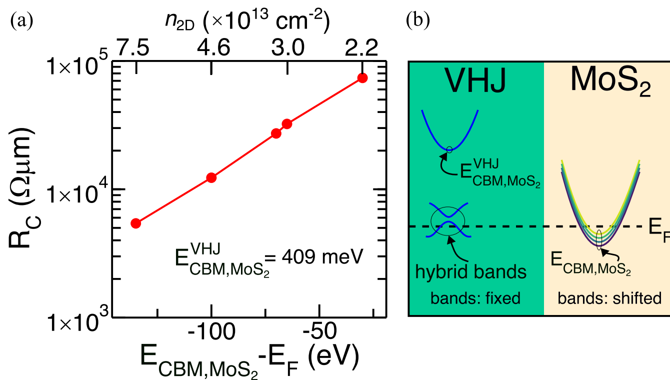

Fig. 5. (a) Calculated contact resistance from NEGF ab initio simulations. Results are obtained by modulating the CBM of the rightmost MoS_2 with respect to E_F, as pictorially shown in (b), thus also modulating the MoS_2 charge density to test the sensitivity to uncertainties in the $n_{2\text{-D}}$ experimental estimate in [13]. The band alignment in the VHJ is fixed by the results from DFT calculations in Fig. 3.

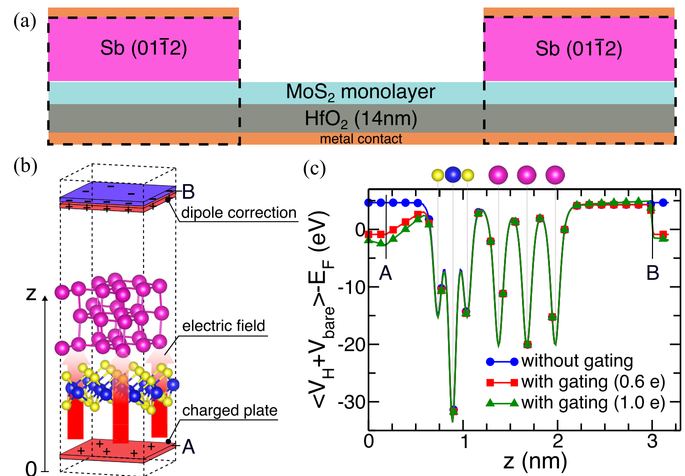

Fig. 6. (a) Sketch of the experimental device in [13], where an HfO_2 back-gate oxide extends under the Sb–MoS_2 VHJ. (b) Simulation setup used in QE to describe the BGB effect to reproduce the VHJ in the dashed region in (a). The charge plate in A is positively charged and red arrows depict the electric field in the MoS_2 and Sb regions. The dipole correction in B allows us to zero the electric field in the vacuum region above Sb, as required by the periodicity along z implied by the plane-wave basis. (c) Average in-plane electrostatic potential (Hartree + bare potentials) either with no gating effect (blue circles) or with increasing values of the charge in the charged plate (squares and triangles). The plot does not show the energy barrier introduced in the vacuum region to prevent electrons spilling from the MoS_2 to the charged plate [17]. Point B indicates the abscissa where the dipole correction is enforced in DFT calculations (see Section II).

reported in experiments [13]. The availability of states around E_F, both in the VHJ and in the external MoS_2 layer [see LDOS plot in Fig. 4(c)], appears insufficient to achieve a low R_C, because the transmission from the hybridized states in the VHJ to the external MoS_2 CBM states is poor.

In order to further test the results of Fig. 4, we considered possible uncertainties in the experimental estimate of $n_{2\text{-D}}$ in the MoS_2 channel region [13]. Fig. 5 reports the calculated R_C by increasing $n_{2\text{-D}}$ up to 7.5×10^{13} cm^{-2}, but R_C can only be modulated in a range of values that remain much larger than the experimental value [13]. This can be attributed to the fact that even though the CBM of the MoS_2 outside the VHJ (located at the Γ point of the supercell first BZ) is degenerate by several tens of millielectron volts (Fig. 5), there are no similar states close to E_F in the hybridized bands of the VHJ, where the states resembling the CBM of MoS_2 are instead located at much higher energy, namely, about 400 meV above E_F.

B. Influence of BGB on VHJ Region and on R_C

The vast discrepancy between the simulated and experimental R_C values shown in Figs. 4 and 5 that mainly stems from the fact that the CBM of the MoS_2 external to the VHJ located at the Γ point (in the first BZ of the supercell) has no counterpart states at E_F in the VHJ [see Fig. 5(b)], has prompted us to re-examine the experimental framework. In the experiments, the back-gate electrode extends under the Sb–MoS_2 contact as shown in Fig. 6(a) and the quoted R_C values for an $n_{2\text{-D}} \approx 1 \div 3 \times 10^{13}$ cm^{-2} correspond to back-gate biases up to $10 \div 15$ V [13]. Thus, an electrostatic doping of the MoS_2 in the VHJ should be also expected. Therefore, we performed DFT simulations including a charged plate as a back gate in the VHJ supercell, as illustrated in Fig. 6(b).

By assuming that most of the back-gate voltage drops across the HfO_2, the charge can be estimated as $Q = \varepsilon_0 \varepsilon_r V_{GS}/t_{ox}$. By taking $\varepsilon_r = 25$ for the 14-nm-thick HfO_2 [20], and dividing by the area of the supercell (1.04 nm^2), a 10-V back bias translates into ~1 electron charge/supercell (e./s.c.). The effect of the gating is shown in Fig. 6(c), where the charged plate is

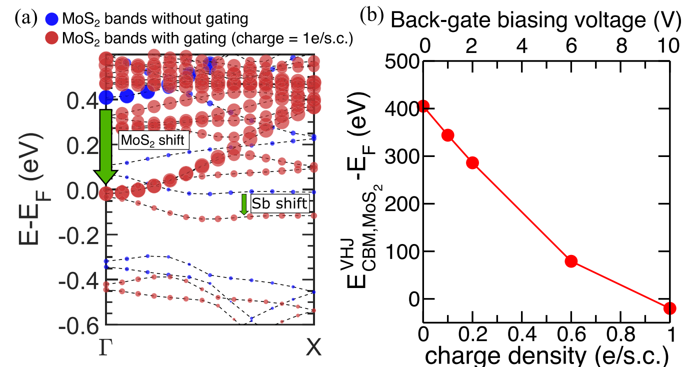

Fig. 7. (a) Influence of the BGB on the band structure of the VHJ. The BGB can effectively pull $E^{\text{VHJ}}_{\text{CBM,MoS}_2}$ at the Γ point toward E_F (see the text and the green line in Fig. 3(a) for the definition of $E^{\text{VHJ}}_{\text{CBM,MoS}_2}$). (b) Difference between $E^{\text{VHJ}}_{\text{CBM,MoS}_2}$ and E_F versus the charge density in the charged plate, which mimics the BGB.

located in A, and a linear average potential drop is observed between the charged plate and the MoS_2 layer (triangular and square symbols). In contrast, a flat potential was observed in the case with no back gating (circles). In these DFT calculations, in order to prevent the electrons from spilling out from the MoS_2 due to the large electric field and the close proximity of the charged plate to the MoS_2, we included a potential barrier between the charged plate and the MoS_2 [17], [21] [not shown in Fig. 6(c)].

Fig. 7(a) shows that the BGB can reduce $E^{\text{VHJ}}_{\text{CBM,MoS}_2}$ by about ≈400 meV, reminding that $E^{\text{VHJ}}_{\text{CBM,MoS}_2}$ is here defined as the CBM at the Γ point for the electronic states of the VHJ projected on the MoS_2 orbitals [see green line in Fig. 3(a)]. The energy shift of Sb states is smaller (~100 meV) compared

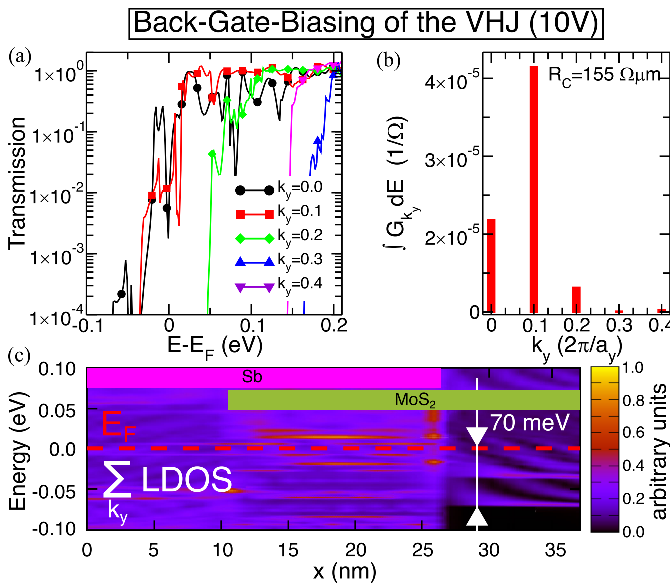

Fig. 8. Same results as shown in Fig. 4, where (a) is the electron transmission $T_{k_y}(E)$ versus energy, (b) is the energy integral of the conductance spectrum defined in (1), and (c) is the LDOS of the system shown in Fig. 1, but here accounting for the BGB effect in the VHJ and for a back-gate voltage of 10 V (corresponding to a charge density of 1 e./s.c. in Fig. 7), which brings $E^{\rm VHJ}_{\rm CBM,MoS_2} \approx -20$ meV below E_F.

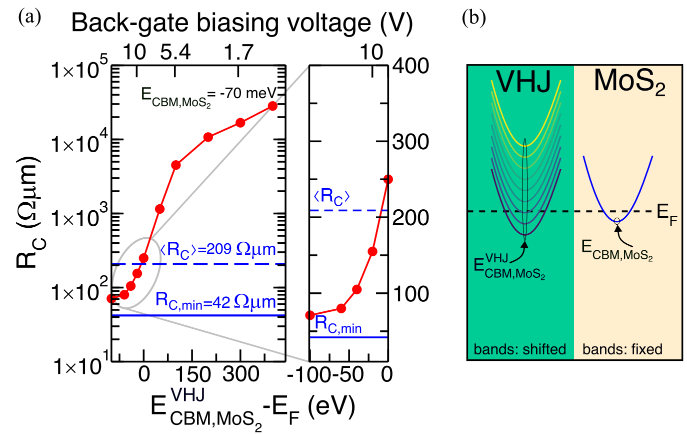

Fig. 9. (a) Calculated contact resistance values obtained from NEGF simulations versus the back-gate voltage or, equivalently, versus the $E^{\rm VHJ}_{\rm CBM,MoS_2}$ alignment to E_F. (b) CBM of the MoS_2 external to the VHJ [see Fig. 1(a)] is fixed at 70 meV below E_F, consistently with the experimental estimate of $n_{\text{2-D}}= 3 \times 10^{13}$ cm^{-2}. The blue solid and dashed lines indicate the lowest and average R_C experimental values reported in [13].

with MoS_2, as expected from the semimetallic nature of Sb. Fig. 7(b) shows that $E^{\rm VHJ}_{\rm CBM,MoS_2}$ crosses E_F for a $V_{\rm GS} \approx 10$ V. The impact of the BGB in the VHJ is further illustrated in Fig. 8(a) and (b), where the transmission and thus the conductance is strongly increased compared with the case with no BGB shown in Fig. 4, leading to a much lower R_C of 155 $\Omega \cdot \mu$m.

It is worth noting that, despite the very similar LDOS in Figs. 4(c) and 8(c) (same color scales), the electronic transmission is very different in Figs. 4(a) and 8(a). This is because the available DOS close to E_F is a necessary but not sufficient condition to reduce the contact resistance, which ultimately requires to have, close to E_F, states of the VHJ that match those in the external MoS_2 region. In this latter respect, Fig. 3(a) shows that the projection onto the MoS_2 orbitals of the states in the VHJ close to E_F is small and, in particular, much smaller than in Fig. 7(a). Clearly, the back gating can pull down to E_F the states of the VHJ that have a good wave function matching to MoS_2, thus resulting in the much better electronic transmission displayed in Fig. 8(a) compared with Fig. 4(a).

To further investigate the R_C dependence on the BGB, that ultimately sets $(E^{\rm VHJ}_{\rm CBM,MoS_2} - E_F)$, in Fig. 9(a) we show the R_C behavior for different gate voltages by keeping fixed the value $n_{\text{2-D}} \approx 3 \times 10^{13}$ cm^{-2} in the external MoS_2 region. This is shown in the sketch of Fig. 9(b), where the band alignment of the MoS_2 in the VHJ is varied while keeping fixed the one of the MoS_2 external to the VHJ. Simulations can reproduce quite well the experimental R_C values with a BGB compatible with experiments, i.e., close to 10 V. A closer inspection of Fig. 9(a) for a BGB ~10 V reveals a large sensitivity of the simulated R_C on the $E^{\rm VHJ}_{\rm CBM,MoS_2}$ value, which depends on the BGB but also on possible uncertainties about the MoS_2 to Sb distance, as it has been reported for the MoS_2-Bi system [12]. These aspects could help explain the spread of the experimentally obtained R_C values [13], besides additional extrinsic effects such as possible MoS_2 defects and trap states.

C. Self-Consistent, 3-D Simulations for a FET Structure

Compared with our previous studies [10], [12], we have extended our ab initio simulator to include a self-consistent coupling between the NEGF and the 3-D Poisson's equation, which allowed us to simulate the monolayer MoS_2 FET with a 20-nm channel length sketched in Fig. 10(a), that resembles the FET shown in Fig. 6(a) [13]. In the device simulations, the semimetallic source contact is described as shown in the previous sections whereas, in order to lighten the heavy computational burden, the drain region is simulated by using a chemical doping of MoS_2 resulting in the same alignment between the Fermi level and the MoS_2 CBM as in the source.

The length of the ab initio simulated source contact is 10 nm, which is twice the transfer length of 5.1 nm estimated from TLM measurements [13]. Given the semimetallic nature of Sb, we neglected the penetration into the source region of the electric field. In other words, we did not solve Poisson's equation in the Sb–MoS_2 VHJ and set Dirichlet-type boundary conditions for Poisson's equation at the source end of the channel [see shaded area in Fig. 10(b)], enforcing the band alignment $(E^{\rm VHJ}_{\rm CBM,MoS_2} - E_F) = -20$ meV. Fig. 10(b) and (c) shows, respectively, the CBM profile along the channel and the spectrum of the current density for a $V_{\rm GS}$ of 0 V and $V_{\rm DS} = 0.1$ V, which is then integrated over the energy to obtain the ballistic $I_{\rm DS}$ current.

Finally, in Fig. 11, we compare the $I_{\rm DS}$ simulations of this work with the experimental data [13], for a $V_{\rm DS} = 0.1$ V. The comparison is performed by subtracting from $V_{\rm GS}$ the threshold voltage V_T, obtained from a linear fitting of the $I_{\rm DS}$ versus $V_{\rm GS}$ curve. We did not attempt a comparison in the subthreshold region because experiments exhibit a subthreshold swing exceeding 200 mV/dec [13], most probably

This article has been accepted for inclusion in a future issue of this journal. Content is final as presented, with the exception of pagination.

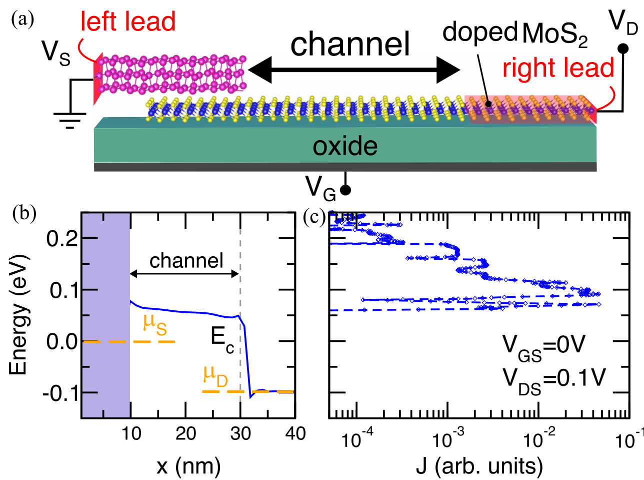

Fig. 10. (a) Sketch of the ab initio simulated short channel MOSFET having a 20-nm channel length and 10-nm contact length (not in scale), where transport calculations include also the Sb–MoS_2 VHJ at the source. An idealized lead is used at the drain to reduce the computational burden. (b) CB minimum profile along the device structure. (c) Current spectrum for $V_{GS} = 0$ V and $V_{DS} = 0.1$ V.

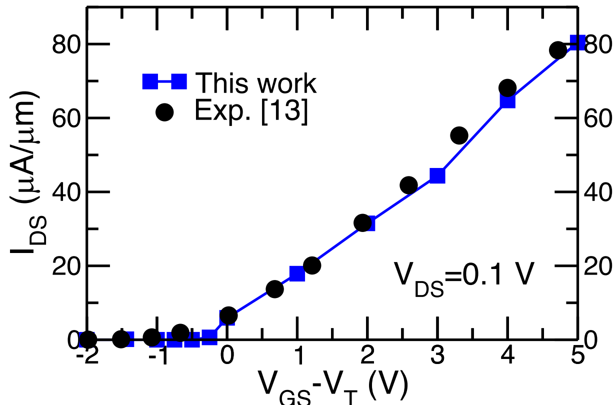

Fig. 11. I_{DS} versus ($V_{GS} - V_T$) characteristics at $V_{DS} = 0.1$ V. Simulated ON-currents for the device shown in Fig. 10(a) agree well with experimental results from Fig. 8(c) in the extended data of [13]. Experiments are plotted versus ($V_{GS} - V_T$) by using $V_T = -4$ V, extracted from a linear fitting of the I_{DS} versus V_{GS} experimental curve.

due to traps in the bandgap of MoS_2 or border traps in the HfO_2 layer [22], whose description goes beyond the scope of this article. Fig. 11 shows that the simulated I_{DS} in the ON state is in good agreement with experiments.

V. Conclusion

The origin of the close to quantum limit resistance of Sb–MoS_2 contacts has been investigated by means of ab initio transport simulations. Our results suggest that the hybridized states in the VHJ are not sufficient to explain the low R_C value that requires to have MoS_2-type states in the VHJ that match the CB minimum of the external MoS_2 layer. This, in turn, can be only attained by accounting for the back-gate biasing, which emphasizes the added value of the ab initio approach to the device modeling that we have embraced in this study.

Finally, we used self-consistent simulations, coupling the NEGF equations with the 3-D Poisson's equation, to analyze a FET structure resembling that reported in [13], and comprising an ab initio description of the Sb–MoS_2 contact at the source. The simulation results agree quite well with experiments in the ON-state operation of the transistor.

References

[1] G. Iannaccone, F. Bonaccorso, L. Colombo, and G. Fiori, "Quantum engineering of transistors based on 2D materials heterostructures," *Nature Nanotechnol.*, vol. 13, no. 3, pp. 183–191, Mar. 2018, doi: 10.1038/s41565-018-0082-6.

[2] M. C. Lemme, D. Akinwande, C. Huyghebaert, and C. Stampfer, "2D materials for future heterogeneous electronics," *Nature Commun.*, vol. 13, no. 1, p. 1392, Mar. 2022, doi: 10.1038/s41467-022-29001-4.

[3] J. Ni, Q. Fu, K. Ostrikov, X. Gu, H. Nan, and S. Xiao, "Status and prospects of ohmic contacts on two-dimensional semiconductors," *Nanotechnology*, vol. 33, no. 6, Nov. 2021, Art. no. 062005, doi: 10.1088/1361-6528/ac2fe1.

[4] W. Cao et al., "The future transistors," *Nature*, vol. 620, no. 7974, pp. 501–515, Aug. 2023, doi: 10.1038/s41586-023-06145-x.

[5] R.-S. Chen, G. Ding, Y. Zhou, and S.-T. Han, "Fermi-level depinning of 2D transition metal dichalcogenide transistors," *J. Mater. Chem. C*, vol. 9, no. 35, pp. 11407–11427, 2021, doi: 10.1039/d1tc01463c.

[6] T. Komesu et al., "Adsorbate doping of MoS_2 and WSe_2: The influence of Na and Co," *J. Phys., Condens. Matter*, vol. 29, no. 28, Jul. 2017, Art. no. 285501, doi: 10.1088/1361-648x/aa7482.

[7] P.-C. Shen et al., "Ultralow contact resistance between semimetal and monolayer semiconductors," *Nature*, vol. 593, no. 7858, pp. 211–217, May 2021, doi: 10.1038/s41586-021-03472-9.

[8] K. P. O'Brien et al., "Advancing 2D monolayer CMOS through contact, channel and interface engineering," in *IEDM Tech. Dig.*, 2021, pp. 1–4, doi: 10.1109/IEDM19574.2021.9720651.

[9] A.-S. Chou et al., "Antimony semimetal contact with enhanced thermal stability for high performance 2D electronics," in *IEDM Tech. Dig.*, 2021, pp. 1–4, doi: 10.1109/IEDM19574.2021.9720608.

[10] D. Lizzit, P. Khakbaz, F. Driussi, M. Pala, and D. Esseni, "Ab-initio transport simulations unveil the Schottky versus tunneling barrier trade-off in metal-TMD contacts," in *IEDM Tech. Dig.*, Dec. 2022, p. 28, doi: 10.1109/IEDM45625.2022.10019449.

[11] A. Kumar et al., "Sub-200 Ω·μm alloyed contacts to synthetic monolayer MoS_2," in *IEDM Tech. Dig.*, Dec. 2021, pp. 1–4, doi: 10.1109/IEDM19574.2021.9720609.

[12] D. Lizzit, P. Khakbaz, F. Driussi, M. Pala, and D. Esseni, "Ohmic behavior in metal contacts to n/p-type transition-metal dichalcogenides: Schottky versus tunneling barrier trade-off," *ACS Appl. Nano Mater.*, vol. 6, no. 7, pp. 5737–5746, Apr. 2023, doi: 10.1021/acsanm.3c00166.

[13] W. Li et al., "Approaching the quantum limit in two-dimensional semiconductor contacts," *Nature*, vol. 613, no. 7943, pp. 274–279, Jan. 2023, doi: 10.1038/s41586-022-05431-4.

[14] *Green-Tea Code*. Accessed: May 2023. [Online]. Available: https://github.com/marcopala/Green-Tea-

[15] M. G. Pala, P. Giannozzi, and D. Esseni, "Unit cell restricted bloch functions basis for first-principle transport models: Theory and application," *Phys. Rev. B, Condens. Matter*, vol. 102, no. 4, Jul. 2020, Art. no. 045410, doi: 10.1103/physrevb.102.045410.

[16] P. Giannozzi et al., "QUANTUM ESPRESSO: A modular and open-source software project for quantum simulations of materials," *J. Phys., Condens. Matter*, vol. 21, no. 39, Sep. 2009, Art. no. 395502, doi: 10.1088/0953-8984/21/39/395502.

[17] P. Giannozzi et al., "Advanced capabilities for materials modelling with quantum ESPRESSO," *J. Phys., Condens. Matter*, vol. 29, no. 46, Nov. 2017, Art. no. 465901, doi: 10.1088/1361-648x/aa8f79.

[18] M. Farmanbar and G. Brocks, "Ohmic contacts to 2D semiconductors through van der Waals bonding," *Adv. Electron. Mater.*, vol. 2, no. 4, Apr. 2016, Art. no. 1500405, doi: 10.1002/aelm.201500405.

[19] T. Märkl et al., "Engineering multiple topological phases in nanoscale van der Waals heterostructures: Realisation of α-antimonene," *2D Mater.*, vol. 5, no. 1, Oct. 2017, Art. no. 011002, doi: 10.1088/2053-1583/aa8d8e.

[20] J. J. Kim et al., "Intrinsic time zero dielectric breakdown characteristics of HfAlO alloys," *IEEE Trans. Electron Devices*, vol. 60, no. 11, pp. 3683–3689, Nov. 2013, doi: 10.1109/TED.2013.2281857.

[21] D. Pierucci et al., "Atomic and electronic structure of trilayer graphene/SiC(0001): Evidence of strong dependence on stacking sequence and charge transfer," *Sci. Rep.*, vol. 6, no. 1, p. 33487, Sep. 2016, doi: 10.1038/srep33487.

[22] S. M. Sze, Y. Li, and K. K. Ng, *Physics of Semiconductor Devices*. Hoboken, NJ, USA: Wiley, 2021.